

Recovering quantum coherence of a cavity qubit through environment monitoring and active feedback

Uri Goldblatt, Nitzan Kahn, Sergey Hazanov, Ofir Milul, Barkay Guttel, Lalit M. Joshi, Daniel Chausovsky, Fabien Lafont, and Serge Rosenblum

Department of Condensed Matter Physics, Weizmann Institute of Science, Rehovot, Israel

Decoherence in qubits, caused by their interaction with a noisy environment, poses a significant challenge to developing reliable quantum processors. Monitoring the qubit's environment enables not only to identify decoherence events but also to reverse these errors, thereby restoring the qubit coherence. This approach is particularly beneficial for superconducting cavity qubits, whose unavoidable interaction with auxiliary transmons impacts their coherence. In this work, we uncover the intricate dynamics of cavity decoherence by tracking the noisy trajectory of a transmon acting as the cavity's environment. Using real-time feedback, we successfully recover the lost coherence of the cavity qubit, achieving a fivefold increase in its dephasing time. Alternatively, by detecting transmon errors and converting them into erasures, we improve the cavity phase coherence by more than an order of magnitude. These advances are essential for implementing long-lived cavity qubits with high-fidelity gates and can enable more efficient bosonic quantum error correction codes.

Achieving long lifetimes of quantum information is crucial for reducing errors in quantum processors. This goal has driven significant advances in the coherence of superconducting quantum circuits [1–9], which are particularly sensitive to noise. Despite these ongoing improvements, interaction with the noisy environment calls for error-mitigation strategies, such as quantum error correction. This approach involves redundantly encoding information across multiple physical qubits [10–12] or in a high-dimensional bosonic system [13–17]. Errors are detected through repeated measurement of the redundant degrees of freedom and corrected using active feedback [10, 11, 13–15, 17, 18]. Alternatively, autonomous quantum error correction uses dissipation to remove the entropy introduced by the errors [19–21]. While quantum error correction can be effective irrespective of the error's origin, it typically entails substantial hardware overheads.

A complementary strategy employing real-time feedback is to monitor noise in the qubit's environment. Auxiliary spectator qubits can be used to probe slow drifts in the qubit's local environment, allowing real-time calibration of gate sequences [22–24]. However, this approach cannot be used to recover quantum information lost through entanglement with a noisy environment, such as frequency noise caused by thermally excited readout resonators [25, 26] or energy exchange with nearby two-level systems [27–29].

Decoherence caused by coupling to a noisy environment presents a particularly significant challenge for bosonic qubits encoded in superconducting cavities [30]. As photon lifetimes of cavity qubits continue to improve [7–9, 31], they become limited by their coupling to noisy elements such as transmon ancillas [30] (Figs. 1a and 1b). While dispersive coupling to a transmon allows for universal control of the cavity qubit [32–35], it also causes thermal transmon excitations to spread to the cavity in the form of frequency shifts. The uncertain durations of the transmon excitations result in random phase accumulations of the cavity state, causing decoherence (Fig. 1c). This shot-noise dephasing process increasingly presents a bottleneck for extending cavity qubit coherence times [6, 7] and for increasing the gain of bosonic quantum error correction schemes [13, 14, 36]. In previous work [37], passive methods

successfully decoupled [38, 39] the transmon ancilla from the cavity qubit, thereby suppressing shot-noise dephasing. How-

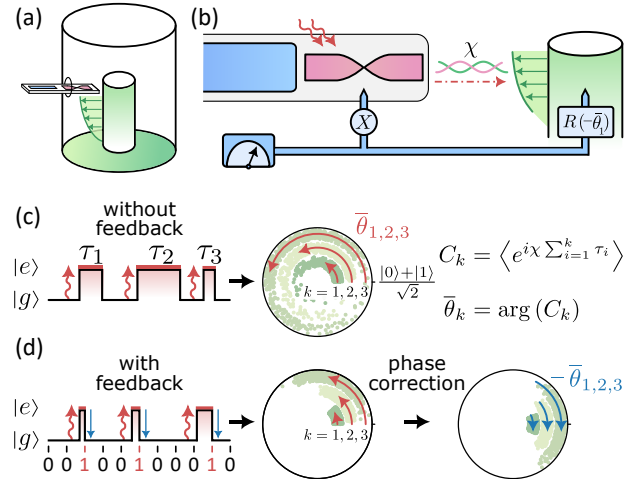


FIG. 1. Decoherence and coherence recovery in a cavity-transmon system. **a**, Depiction of the experimental setup. A cavity mode (green arrows) interacts dispersively with a chip-based transmon ancilla (magenta), which is monitored by a readout resonator (blue rectangle). **b**, Illustration of the feedback protocol. Upon detecting a transmon excitation (red wavy arrows), a reset pulse (X) and a cavity phase correction $R(-\bar{\theta}_1)$ are applied to minimize error propagation to the cavity (red dashed arrow). **c**, Illustration of the cavity qubit decoherence mechanism. Without feedback, each thermal transmon excitation induces a cavity phase shift $\chi\tau_i$, with τ_i the exponentially distributed excitation duration and χ the dispersive interaction rate. As a result, the cavity state evolves from $\frac{1}{\sqrt{2}}(|0\rangle + |1\rangle)$ to $\frac{1}{\sqrt{2}}(|0\rangle + e^{i\theta_k}|1\rangle)$, with $\theta_k = \chi\sum_{i=1}^k \tau_i$ the phase accumulated due to k excitations. The distribution of θ_k is illustrated by individual realizations (green dots) on the equatorial plane of the cavity qubit's Bloch sphere. The uncertainty in θ_k affects the cavity coherence C_k , defined by the ensemble average of $e^{i\theta_k}$. Moreover, the coherence phase $\bar{\theta}_k \equiv \arg(C_k)$ (red arrows) varies with the excitation count k , further contributing to dephasing. **d**, The feedback protocol uses transmon reset pulses to limit excitation durations to the time between measurements, and a trajectory-dependent cavity phase correction $-\bar{\theta}_k = -k\bar{\theta}_1$. Both approaches minimize the cavity phase uncertainty.

ever, the absence of real-time feedback limits the achievable enhancements in cavity qubit coherence times.

Here, we address this challenge by repeatedly measuring the transmon and applying real-time feedback (Fig. 1d). After every measurement, we reset the transmon to the ground state [40], reducing the uncertainty in the duration of the excitations. In addition, we use the measurement outcomes to predict the average phase accumulated by the cavity qubit, allowing us to recover the encoded quantum information. We demonstrate a fivefold improvement in the dephasing time of the cavity qubit and explore the protocol's performance for different measurement intervals and transmon excitation rates. Our observations indicate improved coherence across the entire parameter range. Moreover, the repeated measurements can be used to flag transmon excitations, converting them to cavity qubit erasure errors [41–46]. Postselecting on no erasures, we observe an extension of the cavity dephasing time beyond 100 ms. Besides its application in quantum memories, our approach also holds promise for quantum sensing [47] and quantum computing [42, 43]. For instance, variations of our scheme can be used to realize high-fidelity gates on cavity qubits.

We demonstrate our protocol using a three-dimensional aluminum stub cavity [6] whose fundamental mode has a single-photon lifetime of $T_1^c = 1.57 \pm 0.02$ ms. The transmon qubit, serving as an ancilla, has a lifetime $T_1 = 67.0 \pm 0.3$ μ s, a coherence time $T_2 = 30.0 \pm 0.2$ μ s, and a thermal excited state population $\bar{n}_{\text{th}} = 0.80 \pm 0.05$ %. The transmon is coupled to a readout resonator, enabling high-fidelity single-shot measurement of its state. The transmon enables universal control of the cavity qubit through their dispersive interaction, characterized by the Hamiltonian $\hat{H}/\hbar = -\chi\hat{n}|e\rangle\langle e|$. Here, $\chi/2\pi = 73$ kHz represents the dispersive interaction rate, $|e\rangle$ is the transmon's first excited state, and \hat{n} is the cavity photon number operator. This interaction results in a cavity phase-space rotation $e^{i\chi\tau\hat{n}}$ at an angle proportional to the total time τ the transmon spends in the excited state (which we assume to be classical). Shot noise in the transmon state due to its finite temperature therefore causes the cavity state to decohere.

Before describing our coherence recovery protocol in detail, we first characterize the baseline coherence time of our cavity qubit using a standard Ramsey-type experiment. We initialize the transmon in the state $\frac{1}{\sqrt{2}}(|g\rangle + |e\rangle)$, which we then map to the cavity using a sideband drive [48, 49]. This procedure encodes a superposition of vacuum and the single-photon Fock state $\frac{1}{\sqrt{2}}(|0\rangle + |1\rangle)$ in the cavity. Following varying idle periods, we decode the single-photon qubit by applying the sideband drive a second time. This maps the single-photon qubit back to the transmon, where its coherence can be measured. We observe a baseline cavity coherence time of $T_2^c = 2.24 \pm 0.04$ ms, enabling us to extract a dephasing time $T_\phi^c = (1/T_2^c - 1/2T_1^c)^{-1} = 7.7 \pm 0.3$ ms. The dephasing rate expected from thermal transmon excitations is approximately [50]

$$\Gamma_\phi^c = \Gamma_\uparrow \frac{\chi^2}{\chi^2 + \Gamma^2} \approx \Gamma_\uparrow, \quad (1)$$

with $\Gamma \equiv 1/T_1$ the transmon decay rate. The rate of thermal transmon excitations is $\Gamma_\uparrow \approx \bar{n}_{\text{th}}\Gamma = (8.4 \pm 0.2 \text{ ms})^{-1}$, indicating that these excitations are the dominant cause of cavity dephasing.

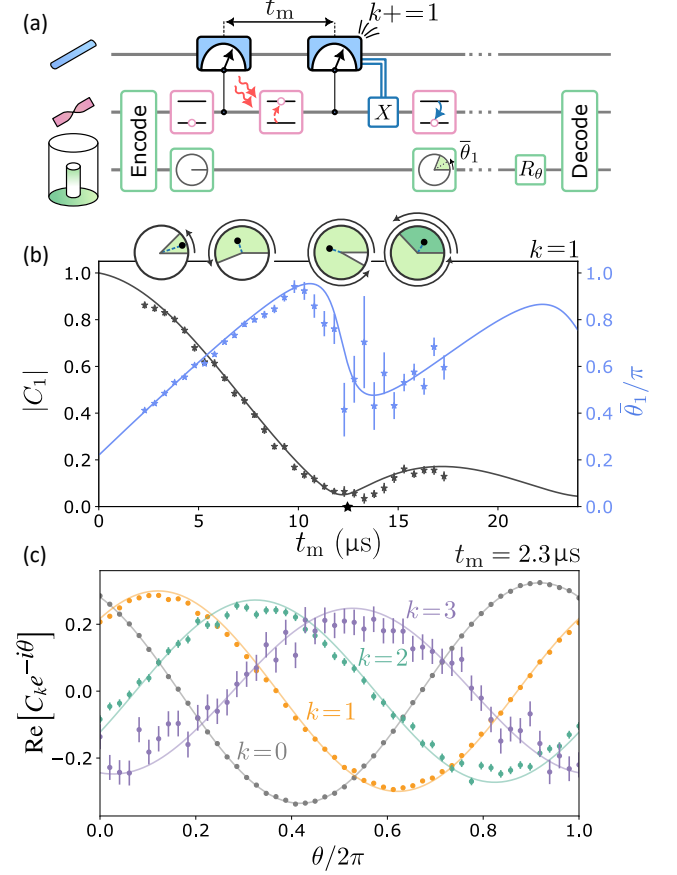


FIG. 2. Characterizing cavity decoherence with repeated transmon measurements. **a**, The characterization circuit first encodes the cavity-transmon system in $\frac{1}{\sqrt{2}}(|0\rangle + |1\rangle) \otimes |g\rangle$. The transmon is repeatedly measured and conditionally reset to $|g\rangle$ at intervals of t_m . The cavity state then undergoes a phase rotation R_θ and is subsequently decoded. **b**, Amplitude $|C_1|$ (black markers) and phase θ_1 (blue markers) of the cavity state coherence as a function of t_m , conditioned on a single detected transmon excitation $k = 1$. The coherence amplitude and phase are displayed relative to their values for $k = 0$. The theoretical model (solid lines) is similar to equation (2), but accounts for transmon decay, achieving a more accurate fit (see Supplementary Section III). The measurement interval corresponding to $t_m = 2\pi/\chi$ is indicated by a black star. The insets illustrate the equatorial plane of the cavity qubit's Bloch sphere with the phase distribution in green and the coherence indicated by a black dot. **c**, Cavity coherence postselected on different observed excitation numbers k at $t = 0.8$ ms. The cavity state is measured along the basis $\frac{1}{\sqrt{2}}(|0\rangle \pm e^{i\theta}|1\rangle)$ with varying θ by applying a rotation R_θ before the decoding (see Methods). The results show that every added excitation shifts the coherence by a fixed phase, and reduces its amplitude by a fixed factor. The photon-loss-limited coherence for $k = 0$ is fitted with a sinusoidal curve, whereas coherences for subsequent excitation numbers are plotted by adding phases $k\theta_1$ and multiplying the amplitude by $|C_1|^k$ (solid lines). The experimental parameters in this figure differ from the rest of the article, with $\chi/2\pi = 82.1$ kHz and $\theta_0 = 0.22\pi$.

As a first step towards addressing shot-noise dephasing, we monitor the transmon in real-time through repeated measurements [51]. Upon detecting an excitation, we reset the transmon to its ground state (Fig. 1d). This procedure limits the duration of excitations to the time between measurements t_m , thereby reducing the cavity dephasing rate.

To analyze the effect of the measurement interval t_m on cavity decoherence, we focus on trajectories with a single detected excitation (Fig. 2a). This excitation induces a cavity phase $\theta_1 = \chi\tau_1$, where the excitation duration τ_1 is uniformly distributed between $[0, t_m]$, ignoring the effect of transmon decay. The resulting cavity coherence $C_1 \equiv \langle e^{i\chi\tau_1} \rangle$, corresponding to the characteristic function of τ_1 , is determined by measuring the cavity along the basis $\frac{1}{\sqrt{2}}(|0\rangle \pm e^{i\theta}|1\rangle)$ with varying θ (see Supplementary Section III and Methods). Fig. 2b shows the measured amplitude $|C_1|$ and phase $\bar{\theta}_1 \equiv \arg(C_1)$ of the cavity coherence as a function of t_m . The results are in agreement with the theoretical prediction (see Supplementary Section II)

$$\begin{aligned} |C_1| &= \left| \text{sinc} \left(\frac{\chi t_m}{2} \right) \right| \\ \bar{\theta}_1 &= \frac{\chi t_m}{2} \bmod \pi + \theta_0, \end{aligned} \quad (2)$$

where we assume transmon decay is negligible, i.e., $\Gamma \ll \chi, t_m^{-1}$. The sinc profile arises because it represents the characteristic function of the uniform distribution. Similarly, $\frac{\chi t_m}{2} \bmod \pi$ corresponds to the mean of the uniform distribution. The offset phase θ_0 is a phenomenological parameter, which we attribute to the differential Stark shift from the measurement pulse when the transmon is excited.

For short measurement intervals $t_m \ll \chi^{-1}$, the coherence can be approximated by $|C_1| \approx 1 - (\chi t_m)^2/24$. In this limit, the excitation duration is too short to appreciably change the cavity phase, implying that frequent transmon measurements can drastically mitigate cavity dephasing. Using a measurement interval of $t_m = 2.6 \mu\text{s}$, the coherence loss due to a single excitation is limited to only 5.8%. In contrast, for $t_m = 2\pi n/\chi$ with $n \in \mathbb{N}$, the phase distribution spans the entire unit circle, fully erasing the cavity coherence.

However, cavity dephasing is not only due to the uncertainty in the duration of individual transmon excitations; the uncertainty in the number of such events also plays an important role (Fig. 1c). The number of excitations k observed up to time t is approximately Poisson distributed with mean and variance given by Γt . The uncertainty in the resulting cavity phase $\theta_k = \chi \sum_{i=1}^k \tau_i$ contributes significantly to cavity dephasing. To evaluate the cavity coherence conditioned on k excitations $C_k \equiv \langle e^{i\theta_k} \rangle$, we use the fact that for sufficiently low excitation rates $\Gamma t \ll \Gamma$, the phases acquired from different excitations are mutually independent. Consequently, this yields $C_k = (C_1)^k$. The observed coherence postselected on k excitations (Fig. 2c) confirms that every added excitation shifts the coherence by a constant phase $\bar{\theta}_1$ and reduces its amplitude by a fixed factor $|C_1|$.

To minimize the decoherence arising from the uncertainty in the number of excitation events, we apply a phase correc-

tion $-\bar{\theta}_k = -k\bar{\theta}_1$ before decoding the cavity state (Fig. 1d), where k is the observed excitation count for each individual experimental sequence. Equivalently, we can apply a phase correction $-\bar{\theta}_1$ in real-time each time an excitation is observed.

Having set up all necessary elements, we proceed to implement the coherence recovery protocol. This protocol involves the repetitive execution of three steps: high-fidelity measurement of the transmon state, conditional reset of the transmon, and conditional correction of the accumulated cavity phase (Fig. 3a). The reset pulse reduces the uncertainty in the duration of each excitation and prevents further excitations to the second excited transmon state $|f\rangle$. The phase correction removes the contribution from the uncertainty in the number of excitations, leaving the residual uncertainty from individual excitations as the only contribution to cavity dephasing. Since the rate of such events is Γ_\uparrow , the coherence recovery protocol is predicted (see Supplementary Section III) to produce a cavity dephasing rate

$$\Gamma_{\phi, \text{fb}}^c = \Gamma_\uparrow \left(1 - \left| \text{sinc} \left(\frac{\chi t_m}{2} \right) \right| \right), \quad (3)$$

yielding an improvement factor of $\Gamma_\phi^c / \Gamma_{\phi, \text{fb}}^c \approx 17$ with respect to the idling case.

An alternative strategy without the need for feedback could be considered, wherein transmon excitations are autonomously dissipated. For example, a parametric drive can transfer the excitation to a lossy resonator, where the energy is quickly dissipated [52]. Although this approach is similar to the application of conditional reset pulses, it is unable to correct for cavity phase accumulations. Consequently, the expected dephasing times are four times lower than those achievable with feedback (see Supplementary Section III).

We evaluate the performance of the feedback protocol by initializing the cavity to $\frac{1}{\sqrt{2}}(|0\rangle + |1\rangle)$, applying the protocol for varying periods, and measuring the remaining coherence. Using our shortest measurement interval $t_m = 2.6 \mu\text{s}$, we find that the coherence time is extended from $T_2^c = 2.24 \pm 0.04 \text{ ms}$ to $2.85 \pm 0.04 \text{ ms}$ (Figs. 2b and 2c). This corresponds to an enhancement of the dephasing time by a factor of 4.5, from $T_\phi^c = 7.7 \pm 0.3 \text{ ms}$ to $T_{\phi, \text{fb}}^c = 35 \pm 4 \text{ ms}$. Though substantial, this improvement does not reach the expected factor of 17. This is primarily due to false positives, where a measurement outcome $|e\rangle$ is incorrectly assigned to a transmon in $|g\rangle$ owing to the finite signal-to-noise ratio of the measurement signal. While these errors induce effective heating events at a high rate of $\frac{p_{e|g}}{t_m} = (11.8 \text{ ms})^{-1}$, where $p_{e|g} = 2.2 \times 10^{-4}$ is the probability of a false-positive error, most of these excitations are captured and corrected in the subsequent measurement round (see Supplementary Section III).

In the context of quantum error-correcting codes, the ability to flag qubit errors can substantially improve error thresholds and code distances [44–46, 53, 54]. Converting transmon excitations into such “erasure errors” of the cavity qubit can therefore be of great benefit, provided that the residual error rate after postselecting on no erasures is substantially smaller than the erasure rate. Excluding all experimental runs

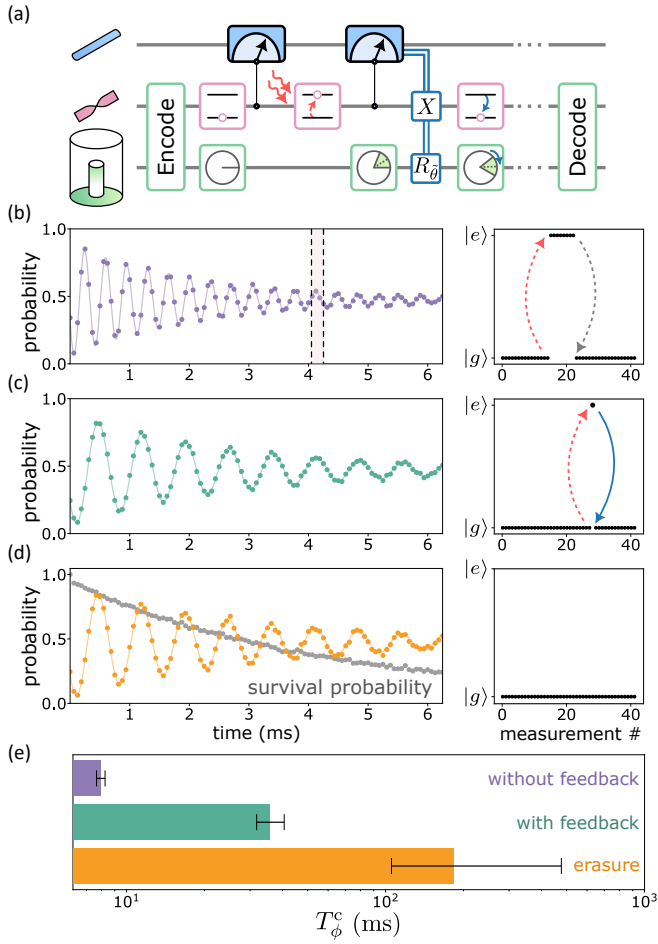


FIG. 3. Enhancing quantum coherence through monitoring and feedback. **a**, Circuit for the coherence recovery protocol, involving the application of a transmon measurement followed by a conditional reset pulse X and cavity phase correction R_{θ} in a repetitive cycle with measurement interval $t_m = 2.6 \mu\text{s}$. **b-d**, The left panels show the probability of measuring the transmon in $|e\rangle$ after the decoding sequence, yielding cavity coherence decay curves. The right panels display representative transmon trajectories taken from a short segment of the experiment (shaded area). Spontaneous excitation (relaxation) events are shown by red (gray) arrows, while the active reset operation is depicted by a blue arrow. We compare outcomes for three cases: **b**, without measurement and feedback, **c**, with both measurement and feedback, choosing a correction phase θ that maximizes the coherence, and **d**, removing erasure errors, i.e., keeping only experimental shots without observed transmon excitations. The derived coherence times are 2.24 ± 0.04 ms, 2.85 ± 0.04 ms, and 3.10 ± 0.06 ms, respectively. Measuring the fraction of experimental shots that survive after post-selection (gray markers) reveals an exponentially decaying survival probability with erasure rate $(4.43 \text{ ms})^{-1}$. **e**, Comparison of dephasing times for the three cases, indicating an improvement from 7.7 ± 0.3 ms for the no-feedback case to 35 ± 4 ms with feedback. Postselecting on no erasures further enhances the dephasing time to 182_{-78}^{+292} ms (see Methods).

in which transmon excitations were observed, we obtain a coherence time of 3.10 ± 0.06 ms, close to the $2T_1^c$ limit imposed by single-photon loss (Fig. 3d). The corresponding dephasing time is $T_{\phi, \text{ps}}^c = 182_{-78}^{+292}$ ms (see Methods). We attribute the remaining dephasing to shot-noise cavity dephasing induced by the measurement pulses. The observed erasure rate

$(4.43 \text{ ms})^{-1}$ is in agreement with the expected excitation rate of $\frac{P_{\text{elg}}}{t_m} + \Gamma_{\uparrow} = (4.7 \text{ ms})^{-1}$. The erasure rate is, therefore, a factor of 41 larger than the dephasing rate after postselecting on no erasures, confirming that the cavity qubit possesses the necessary hierarchy of error rates for its application as an erasure qubit.

We next examine the robustness of the coherence recovery protocol by characterizing its performance across a range of experimental parameters. First, we characterize the dephasing rate as a function of the thermal excitation rate, both with and without applying the feedback protocol. We achieve this by applying a weak incoherent transmon drive with varying power, thereby inducing an effective transmon heating mechanism (see Methods). For sufficiently small thermal populations, we expect the dephasing rate to be linear [39] in the thermal excitation rate (see equations (1) and (3)). In fact, for the idling case, we observe that the dephasing rate approximately equals the heating rate (Fig. 4a). This is expected, since in the limit $\chi \gg \Gamma$, every transmon excitation completely decoheres the cavity state (see equation (1)). The data for the feedback

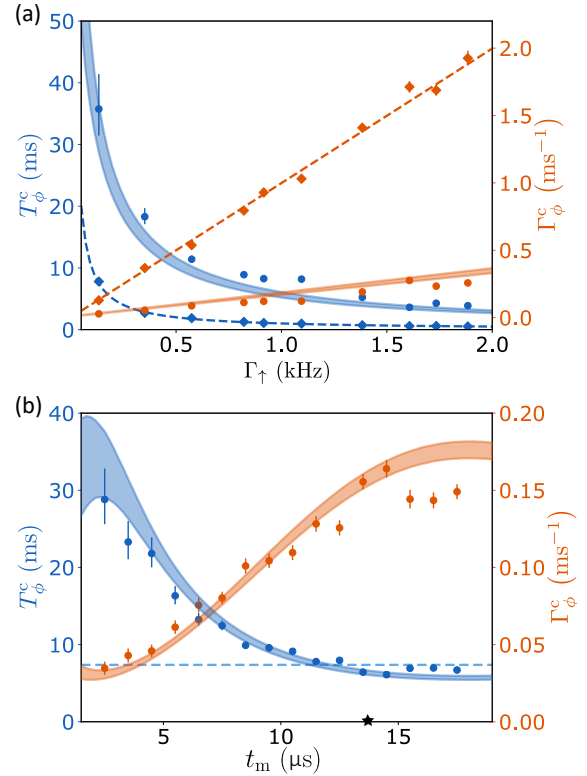


FIG. 4. Performance of the feedback protocol. **a**, Cavity dephasing times T_{ϕ}^c (blue) and rates $\Gamma_{\phi}^c = 1/T_{\phi}^c$ (orange) for various transmon heating rates without measurement and feedback (diamond markers) and with measurement and feedback (circles) using $t_m = 2.6 \mu\text{s}$. The theoretical models are shown with dashed and solid lines for the idling and feedback cases, respectively (see Supplementary Section IV). The shading indicates the uncertainty in the experimental parameters. **b**, Cavity dephasing times (blue) and rates (orange) as a function of the measurement interval t_m . The dephasing time for an idling cavity qubit is shown by a dashed blue line. The black star denotes the measurement interval corresponding to $t_m = 2\pi/\chi$.

case also matches the expected linear dependence on the excitation rate. The ratio of the two slopes indicates a factor of 7.3 improvement in the dephasing times using the coherence recovery protocol. This improvement exceeds the one observed without inducing transmon heating, as higher excitation rates reduce the significance of false positive errors and measurement-induced cavity dephasing.

Next, we investigate the performance of the protocol for varying measurement intervals t_m . For this experiment, we choose a correction phase of $\chi t_m/2$. While this phase is optimal for short measurement intervals, it deviates from the optimal phase for $t_m \gtrsim \chi^{-1}$. The observed results agree with the expected behavior (Fig. 4b). Peak performance is achieved at the highest measurement rate. Further increasing the measurement rate would result in diminishing returns and eventually degrade the coherence, as measurement-induced cavity dephasing and false positive errors start to dominate. Conversely, for lower measurement rates, the residual uncertainty per excitation event grows, leading to increased dephasing rates. When the measurement rate is below χ , the phase correction deviates by more than $\pi/2$ from the optimal phase, resulting in a dephasing rate higher than that of the idling case.

In this work, we have demonstrated a significant enhancement in the dephasing time of cavity qubits by monitoring the coupled transmon ancilla and applying real-time feedback. The protocol effectively mitigates dephasing errors across a wide range of experimental parameters. The coherence enhancement is even more pronounced if detected excitations are treated as erasure errors. One promising improvement is to decide in real time whether to treat a detected transmon error as an erasure error, or whether to attempt correcting the

cavity state. This method could reduce the erasure rate without significantly increasing computational errors. The results could be further improved by using a state estimation algorithm that takes into account the observation history, as opposed to a decision based only on the current measurement (see Supplementary Section VI). This could be used to tailor optimized correction phases for a wider range of identified events, such as measurement errors.

The current demonstration focuses on improving coherence for idling periods, during which the transmon ancilla is expected to remain in its ground state. However, our approach can also be adapted to enhance the fidelities of single-qubit and two-qubit gates on the cavity, during which the transmon may be partially excited [42, 43]. While the protocol was shown for a single-photon qubit encoding, it can also be applied to multiphoton qubits, potentially solving a major bottleneck in bosonic quantum error correction. Given the long single-photon lifetimes of recently demonstrated cavities [9], monitoring the transmon and reversing or erasing dephasing errors could lead to unprecedented quantum memory lifetimes, gate fidelities, and bosonic error correction gains.

ACKNOWLEDGMENTS

We acknowledge valuable input from Vladimir Sivak, Alec Eickbusch, Ofer Zeitouni, and Barak Zackay. We acknowledge financial support from the Israel Science Foundation ISF Quantum Science and Technologies Grants 963/19 and 2022/20, and the European Research Council Starting Investigator Grant Q-CIRC 134847. S.R. is the incumbent of the Rabbi Dr. Roger Herst Career Development Chair.

-
- [1] Place, A. P. *et al.* New material platform for superconducting transmon qubits with coherence times exceeding 0.3 milliseconds. *Nat. Commun.* **12**, 1–6 (2021).
 - [2] Wang, C. *et al.* Towards practical quantum computers: transmon qubit with a lifetime approaching 0.5 milliseconds. *npj Quantum Inf.* **8**, 1–6 (2022).
 - [3] Manucharyan, V. E., Koch, J., Glazman, L. I. & Devoret, M. H. Fluxonium: Single cooper-pair circuit free of charge offsets. *Science* **326**, 113–116 (2009).
 - [4] Grünhaupt, L. *et al.* Granular aluminium as a superconducting material for high-impedance quantum circuits. *Nat. Mater.* **18**, 816–819 (2019).
 - [5] Somoroff, A. *et al.* Millisecond coherence in a superconducting qubit. *Phys. Rev. Lett.* **130**, 267001 (2023).
 - [6] Reagor, M. *et al.* Quantum memory with millisecond coherence in circuit QED. *Phys. Rev. B* **94**, 014506 (2016).
 - [7] Chakram, S. *et al.* Seamless High-Q Microwave Cavities for Multimode Circuit Quantum Electrodynamics. *Phys. Rev. Lett.* **127**, 107701 (2021).
 - [8] Romanenko, A. *et al.* Three-Dimensional Superconducting Resonators at $T < 20$ mK with Photon Lifetimes up to $\tau = 2$ s. *Phys. Rev. Appl.* **13**, 34032 (2020).
 - [9] Milul, O. *et al.* Superconducting Cavity Qubit with Tens of Milliseconds Single-Photon Coherence Time. *PRX Quantum* **4**, 030336 (2023).
 - [10] Krinner, S. *et al.* Realizing repeated quantum error correction in a distance-three surface code. *Nature* **605**, 669–674 (2022).
 - [11] Acharya, R. *et al.* Suppressing quantum errors by scaling a surface code logical qubit. *Nature* **614**, 676–681 (2023).
 - [12] Zhao, Y. *et al.* Realization of an Error-Correcting Surface Code with Superconducting Qubits. *Phys. Rev. Lett.* **129**, 030501 (2022).
 - [13] Ofek, N. *et al.* Extending the lifetime of a quantum bit with error correction in superconducting circuits. *Nature* **536**, 441–445 (2016).
 - [14] Campagne-Ibarcq, P. *et al.* Quantum error correction of a qubit encoded in grid states of an oscillator. *Nature* **584**, 368–372 (2020).
 - [15] Sivak, V. V. *et al.* Real-time quantum error correction beyond break-even. *Nature* **616**, 50–55 (2023).
 - [16] Hu, L. *et al.* Quantum error correction and universal gate set operation on a binomial bosonic logical qubit. *Nat. Phys.* **15** (2019).
 - [17] Ni, Z. *et al.* Beating the break-even point with a discrete-variable-encoded logical qubit. *Nature* **616**, 56–60 (2023).
 - [18] Andersen, C. K. *et al.* Repeated quantum error detection in a surface code. *Nat. Phys.* **16**, 875–880 (2020).
 - [19] Lescanne, R. *et al.* Exponential suppression of bit-flips in a

- qubit encoded in an oscillator. *Nat. Phys.* **16**, 509–513 (2020).
- [20] Li, Z. *et al.* Autonomous error correction of a single logical qubit using two transmons. *Nat. Commun.* **15**, 1681 (2024).
- [21] Gertler, J. M. *et al.* Protecting a bosonic qubit with autonomous quantum error correction. *Nature* **590**, 243–248 (2021).
- [22] Majumder, S., Andreta de Castro, L. & Brown, K. R. Real-time calibration with spectator qubits. *npj Quantum Inf.* **6** (2020).
- [23] Gupta, R. S., Edmunds, C. L., Milne, A. R., Hempel, C. & Biercuk, M. J. Adaptive characterization of spatially inhomogeneous fields and errors in qubit registers. *npj Quantum Inf.* **6** (2020).
- [24] Lingenfelter, A. & Clerk, A. A. Surpassing spectator qubits with photonic modes and continuous measurement for Heisenberg-limited noise mitigation. *npj Quantum Inf.* **9**, 1–15 (2023).
- [25] Gambetta, J. *et al.* Qubit-photon interactions in a cavity: Measurement-induced dephasing and number splitting. *Phys. Rev. A* **74**, 042318 (2006).
- [26] Rigetti, C. *et al.* Superconducting qubit in a waveguide cavity with a coherence time approaching 0.1 ms. *Phys. Rev. B* **86**, 100506 (2012).
- [27] Shalibo, Y. *et al.* Lifetime and coherence of two-level defects in a Josephson junction. *Phys. Rev. Lett.* **105**, 177001 (2010).
- [28] Müller, C., Cole, J. H. & Lisenfeld, J. Towards understanding two-level-systems in amorphous solids: insights from quantum circuits. *Rep. Prog. Phys.* **82**, 124501 (2019).
- [29] Burnett, J. J. *et al.* Decoherence benchmarking of superconducting qubits. *npj Quantum Inf.* **5**, 1–8 (2019).
- [30] Joshi, A., Noh, K. & Gao, Y. Y. Quantum information processing with bosonic qubits in circuit QED. *Quantum Science and Technology* **6**, 033001 (2021).
- [31] Heidler, P. *et al.* Non-Markovian Effects of Two-Level Systems in a Niobium Coaxial Resonator with a Single-Photon Lifetime of 10 milliseconds. *Phys. Rev. Appl.* **16**, 034024 (2021).
- [32] Heeres, R. W. *et al.* Implementing a universal gate set on a logical qubit encoded in an oscillator. *Nat. Commun.* **8**, 94 (2017).
- [33] Krastanov, S. *et al.* Universal control of an oscillator with dispersive coupling to a qubit. *Phys. Rev. A* **92**, 040303 (2015).
- [34] Eickbusch, A. *et al.* Fast universal control of an oscillator with weak dispersive coupling to a qubit. *Nat. Phys.* **18** (2022).
- [35] Diring, A. A., Blumenthal, E., Grinberg, A., Jiang, L. & Hacohe-Gourgy, S. Conditional-not displacement: Fast multioscillator control with a single qubit. *Phys. Rev. X* **14**, 011055 (2024).
- [36] Cai, W., Ma, Y., Wang, W., Zou, C. L. & Sun, L. Bosonic quantum error correction codes in superconducting quantum circuits. *Fundamental Research* **1**, 50–67 (2021).
- [37] Rosenblum, S. *et al.* Fault-tolerant detection of a quantum error. *Science* **361**, 266–270 (2018).
- [38] Zhang, G., Liu, Y., Raftery, J. J. & Houck, A. A. Suppression of photon shot noise dephasing in a tunable coupling superconducting qubit. *npj Quantum Inf.* **3**, 1–4 (2017).
- [39] Yan, F. *et al.* The flux qubit revisited to enhance coherence and reproducibility. *Nat. Commun.* **7**, 12964 (2016).
- [40] Ristè, D., Bultink, C. C., Lehnert, K. W. & Dicarlo, L. Feedback control of a solid-state qubit using high-fidelity projective measurement. *Phys. Rev. Lett.* **109**, 240502 (2012).
- [41] Wu, Y., Kolkowitz, S., Puri, S. & Thompson, J. D. Erasure conversion for fault-tolerant quantum computing in alkaline earth Rydberg atom arrays. *Nat. Commun.* **13**, 1–7 (2022).
- [42] Tsunoda, T. *et al.* Error-Detectable Bosonic Entangling Gates with a Noisy Ancilla. *PRX Quantum* **4**, 020354 (2023).
- [43] Teoh, J. D. *et al.* Dual-rail encoding with superconducting cavities. *PNAS* **120**, e2221736120 (2023).
- [44] Koottandavida, A. *et al.* Erasure detection of a dual-rail qubit encoded in a double-post superconducting cavity (2023). Preprint at <https://arxiv.org/abs/2311.04423>.
- [45] Chou, K. S. *et al.* Demonstrating a superconducting dual-rail cavity qubit with erasure-detected logical measurements (2023). Preprint at <https://arxiv.org/abs/2307.03169>.
- [46] Levine, H. *et al.* Demonstrating a long-coherence dual-rail erasure qubit using tunable transmons. *Phys. Rev. X* **14**, 011051 (2024).
- [47] Niroula, P. *et al.* Quantum Sensing with Erasure Qubits (2023). Preprint at <https://arxiv.org/abs/2310.01512>.
- [48] Pechal, M. *et al.* Microwave-controlled generation of shaped single photons in circuit quantum electrodynamics. *Phys. Rev. X* **4**, 041010 (2014).
- [49] Rosenblum, S. *et al.* A CNOT gate between multiphoton qubits encoded in two cavities. *Nat. Commun.* **9**, 1–6 (2018).
- [50] Wang, Z. *et al.* Cavity Attenuators for Superconducting Qubits. *Phys. Rev. Appl.* **11**, 014031 (2019).
- [51] Murch, K. W., Weber, S. J., Macklin, C. & Siddiqi, I. Observing single quantum trajectories of a superconducting quantum bit. *Nature* **502**, 211–214 (2013).
- [52] Magnard, P. *et al.* Fast and Unconditional All-Microwave Reset of a Superconducting Qubit. *Phys. Rev. Lett.* **121**, 060502 (2018).
- [53] Stace, T. M., Barrett, S. D. & Doherty, A. C. Thresholds for topological codes in the presence of loss. *Phys. Rev. Lett.* **102** (2009).
- [54] Kubica, A. *et al.* Erasure qubits: Overcoming the T_1 limit in superconducting circuits. *Phys. Rev. X* **13** (2022).

METHODS

Measuring the cavity coherence

The coherence of the cavity is characterized by measuring it along the basis $|\psi_\theta^\pm\rangle \equiv \frac{1}{\sqrt{2}}(|0\rangle \pm e^{i\theta}|1\rangle)$ with varying θ . This is achieved by adjusting the phase of the sideband drive in the decoding sequence and then measuring the transmon in the computational basis. The probability of observing $|\psi_\theta^+\rangle$ is given by

$$P_\theta \equiv \text{Tr}(\rho |\psi_\theta^+\rangle\langle\psi_\theta^+|) = \frac{1 + \text{Re}\{\mathcal{C}e^{-i\theta}\}}{2} = \frac{1 + |\mathcal{C}|\cos(\bar{\theta} - \theta)}{2},$$

where the cavity coherence \mathcal{C} is defined by the off-diagonal element of the cavity's density matrix ρ . The coherence amplitude $|\mathcal{C}|$ and phase $\bar{\theta} \equiv \arg(\mathcal{C})$ are determined by fitting the data for $2P_\theta - 1 = \text{Re}\{\mathcal{C}e^{-i\theta}\}$ for varying θ to a sinusoidal curve. This yields

$$|\mathcal{C}| = \max_\theta |2P_\theta - 1|$$

$$\bar{\theta} = \arg \max_\theta (2P_\theta - 1).$$

Similarly, the coherence conditioned on observing k excitations, denoted by C_k , is obtained by postselecting the measured data P_θ on observing k excitations and fitting the resulting data (see Fig. 2c).

System characterization during measurements

For each experiment in which the transmon is monitored, we use a Hidden Markov Model (HMM) to extract the transmon

decay rate Γ , the excitation rate Γ_{\uparrow} , and the false-positive and false-negative probabilities $p_{e|g}$ and $p_{g|e}$ (see Supplementary Section VI). In addition, we use the HMM to calibrate the drive power for achieving a desired effective heating rate in Fig. 4a.

Estimation of Dephasing times

We apply Bayesian Inference to estimate the cavity dephasing times T_{ϕ}^c , using data from lifetime (T_1^c) experiments and Ramsey (T_2^c) experiments. This method involves selecting prior distributions for both the cavity dephasing and decay rates, which we assume to be non-negative. We choose uniform distributions for these priors, yielding conservative estimates of the dephasing times.

SUPPLEMENTARY INFORMATION

I. DEVICE SPECIFICATION

The experimental device is comprised of three elements: a cavity, a transmon qubit, and a readout resonator. The cavity is made from 5N5 aluminum and has a coaxial stub geometry. The cavity was etched to remove contaminants and surface damage introduced by the machining. The aluminum transmon qubit and readout resonator are fabricated on a sapphire chip using electron beam evaporation. The chip is inserted into a coaxial waveguide connected to the cavity, and accessed through input and output couplers in the coaxial waveguide. The device is placed inside a thermalized Oxygen-Free High Conductivity (OFHC) copper shield and encapsulated by an Amumetal 4K (A4K) magnetic shield (see Fig. 10 at the end of the Supplementary Information).

II. DEVICE HAMILTONIAN AND PARAMETERS

We can express the free evolution of the system using the following Hamiltonian:

$$\hat{H} = \omega_r \hat{r}^\dagger \hat{r} + \omega_q \hat{q}^\dagger \hat{q} + \omega_c \hat{c}^\dagger \hat{c} - \frac{K_r}{2} \hat{r}^{\dagger 2} \hat{r}^2 - \frac{K_q}{2} \hat{q}^{\dagger 2} \hat{q}^2 - \frac{K_c}{2} \hat{c}^{\dagger 2} \hat{c}^2 - \chi \hat{c}^\dagger \hat{c} \hat{q}^\dagger \hat{q} - \chi_{qr} \hat{r}^\dagger \hat{r} \hat{q}^\dagger \hat{q} - \chi_{cr} \hat{r}^\dagger \hat{r} \hat{c}^\dagger \hat{c},$$

where $\hat{r}, \hat{q}, \hat{c}$ are the annihilation operators of the readout, transmon, and cavity modes, respectively. The values of the parameters are listed in Table I.

III. ANALYSING CAVITY DECOHERENCE CAUSED BY A NOISY TRANSMON

In this section, we examine the coherence of a cavity initially prepared in $\frac{1}{\sqrt{2}}(|0\rangle + |1\rangle)$ and dispersively coupled to a noisy transmon. We ignore cavity photon loss and focus only on the phase accumulation due to transmon excitations. In a single experimental shot, the cavity evolves to $|\psi_\theta\rangle = \frac{1}{\sqrt{2}}(|0\rangle + e^{i\theta} |1\rangle)$, where the total accumulated phase is $\theta = \chi\tau$ with τ the total

parameter	description	value
$\omega_c/2\pi$	cavity resonance frequency	4.45 GHz
T_1^c	cavity single-photon lifetime	1.57 ± 0.02 ms
T_2^c	cavity coherence time	2.24 ± 0.04 ms
$K_c/2\pi$	cavity anharmonicity	14.3 ± 0.7 Hz (*)
$\chi/2\pi$	cavity-transmon dispersive shift	73.06 ± 0.06 kHz
$\chi_{cr}/2\pi$	cavity-readout dispersive shift	552 ± 18 Hz (*)
$\omega_q/2\pi$	transmon resonance frequency	3.93 GHz
$K_q/2\pi$	transmon anharmonicity	128 MHz
T_1	transmon lifetime	67.0 ± 0.3 μ s (31.5 \pm 1.0 μ s)
T_2	transmon coherence time	29.97 ± 0.19 μ s
T_{2E}	transmon Hahn-echo coherence time	68 ± 1 μ s
\bar{n}_{th}	transmon average thermal population	0.80 ± 0.05 % (0.43 \pm 0.04 %)
Γ_\uparrow	transmon excitation rate	119 ± 5 Hz (134 \pm 11 Hz)
$\chi_{qr}/2\pi$	transmon-readout dispersive shift	1.44 ± 0.02 MHz
$\omega_r/2\pi$	readout resonance frequency	7.83 GHz
T_r	readout lifetime	607 ± 8 ns
$K_r/2\pi$	readout anharmonicity	4.9 ± 0.2 kHz (*)

TABLE I. System parameters and their respective values. Values in parentheses indicate parameters in the presence of repetitive measurements, extracted using a hidden Markov model (see Section VI). In addition, values obtained through simulation, rather than direct measurement, are indicated with an asterisk.

duration the transmon spent in $|e\rangle$ along its trajectory. The accumulated phase θ is drawn from a random variable $\Theta = \chi T$ with probability distribution $f_{\Theta}(\theta) = \chi f_T(\tau)$. We can express the density matrix of the cavity after tracing out the transmon degrees of freedom as an ensemble of different phase accumulations:

$$\rho = \int |\psi_{\chi\tau}\rangle \langle \psi_{\chi\tau}| f_T(\tau) d\tau.$$

We define the cavity state coherence \mathcal{C} as the off-diagonal element of the cavity's density matrix

$$\mathcal{C} \equiv \rho_{10} = \int \langle 1|\psi_{\chi\tau}\rangle \langle \psi_{\chi\tau}|0\rangle f_T(\tau) d\tau = \langle e^{i\chi T} \rangle.$$

The last equality suggests that we can interpret the coherence as the characteristic function of T .

A. Deriving the cavity coherence

We consider the scenario where the transmon is subjected to periodic measurements at intervals of t_m , followed by a reset to the ground state if an excitation is detected. A key realization is that the random variables T_i corresponding to the excited state durations in measurement intervals indexed by i are independent and identically distributed due to the reset operation. As such, we can write for the coherence at time t :

$$\mathcal{C}(t) = \langle e^{i\chi \sum_{i=1}^{t/t_m} T_i} \rangle = \langle \prod_{i=1}^{t/t_m} e^{i\chi T_i} \rangle = \prod_{i=1}^{t/t_m} \langle e^{i\chi T_i} \rangle = C^{t/t_m} = e^{\frac{\ln(C)}{t_m} t}, \quad (4)$$

where $C \equiv \langle e^{i\chi T_1} \rangle$ is the coherence after a single measurement interval. If the decoherence during a single measurement interval is small, we can approximate the cavity dephasing rate by $\Gamma_{\phi, \text{fb}}^c = -\text{Re}(\ln(C))/t_m \approx (1 - \text{Re}(C))/t_m$.

Next, we consider that within a single measurement period, several mutually exclusive events can occur, each with its own associated coherence $C^{(j)}$ and probability of occurrence p_j . We can therefore write $C = \sum_j p_j C^{(j)}$. The dephasing rate is then

$$\Gamma_{\phi, \text{fb}}^c \approx \frac{1}{t_m} \left(1 - \sum_j p_j \text{Re}(C^{(j)}) \right) = \sum_j p_j \left(1 - \text{Re}(C^{(j)}) \right) / t_m = \sum_j \Gamma_{\phi, j}^c, \quad (5)$$

where $\Gamma_{\phi, j}^c \equiv \frac{1}{t_m} p_j \left(1 - \text{Re}(C^{(j)}) \right)$ is the contribution of the j^{th} dephasing mechanism to the total cavity dephasing. We now enumerate the possible events and derive their associated coherences and probabilities. In the current section, we assume a simplified model with only transmon excitation and decay events. In the next section, we will include measurement errors and other imperfections. We assume $\Gamma_{\uparrow} t_m \ll 1$ throughout the derivation. This is a valid assumption for our setup, in which $\Gamma_{\uparrow} t_m = 3 \times 10^{-4}$. We can, therefore, assume that at most one excitation event occurs within a single measurement interval, reducing the number of possible events during a measurement interval to three:

0. No excitation occurs, and coherence is fully maintained, i.e., $C^{(0)} = 1$. This happens with probability $p_0 = 1 - \Gamma_{\uparrow} t_m$. The corresponding dephasing rate is zero: $\Gamma_{\phi, 0}^c = 0$.
1. The transmon is excited, and remains in $|e\rangle$ until it is reset at $t = t_m$. Since $\Gamma_{\uparrow} t_m \ll 1$, the excitation probability is uniformly distributed over the interval. The probability density function for the excitation duration T_1 taking a value $\tau_1 \in [0, t_m]$ is obtained by multiplying the probability density Γ_{\uparrow} of an excitation event at $t_m - \tau_1$ with the probability of no subsequent decay:

$$f_{T_1}^{(1)}(\tau_1) = \frac{1}{p_1} \Gamma_{\uparrow} e^{-\Gamma \tau_1},$$

where we normalize by p_1 , representing the total probability of this event:

$$p_1 = \int_{\tau_1=0}^{t_m} \Gamma_{\uparrow} e^{-\Gamma \tau_1} d\tau_1 = \Gamma_{\uparrow} t_m \frac{1 - e^{-\Gamma t_m}}{\Gamma}.$$

The corresponding cavity state coherence is

$$\begin{aligned} C^{(1)} &= \langle e^{i\chi T_1} \rangle e^{i(\tilde{\theta} + \theta_0)} = e^{i(\tilde{\theta} + \theta_0)} \int_{\tau=0}^{t_m} e^{i\chi \tau_1} f_{T_1}^{(1)}(\tau_1) d\tau_1 \\ &= \frac{\Gamma_{\uparrow} t_m e^{(i\chi - \Gamma)t_m} - 1}{p_1 (i\chi - \Gamma)t_m} e^{i(\tilde{\theta} + \theta_0)}. \end{aligned}$$

Here, we added the feedback phase $\tilde{\theta}$ applied upon detection of the excitation, as well as a phenomenological offset phase θ_0 . Such an offset phase could result from a differential cavity Stark shift between the ground and excited states in the presence of a measurement drive.

The absolute value of the cavity coherence and its phase

$$|C^{(1)}| = \frac{\Gamma t_m}{1 - e^{-\Gamma t_m}} \sqrt{\frac{[e^{-\Gamma t_m} \cos(\chi t_m) - 1]^2 + [e^{-\Gamma t_m} \sin(\chi t_m)]^2}{(\chi^2 + \Gamma^2) t_m^2}}, \quad (6)$$

$$\bar{\theta}^{(1)} = \tan^{-1} \left(\frac{\chi [e^{-\Gamma t_m} \cos(\chi t_m) - 1] + \Gamma e^{-\Gamma t_m} \sin(\chi t_m)}{\Gamma [e^{-\Gamma t_m} \cos(\chi t_m) - 1] - \chi e^{-\Gamma t_m} \sin(\chi t_m)} \right) + \tilde{\theta} + \theta_0 \quad (7)$$

were used as the theoretical model for the data in Fig. 2b of the main text, which postselects on the occurrence of this event. The dephasing rate due to this event is minimized by choosing an optimal feedback phase $\tilde{\theta}_{\text{opt}}$ such that $\bar{\theta}^{(1)} = 0$, yielding $\Gamma_{\phi,1}^c = \frac{1}{t_m} p_1 (1 - |C^{(1)}|)$.

Since the probability distribution of the excitation duration $f_{T_1}^{(1)}(\tau_1)$ is a multiplication of a uniform distribution and an exponential distribution, the coherence can be interpreted as a convolution of the characteristic functions of these distributions, i.e. $C^{(1)} = e^{i(\tilde{\theta} + \theta_0)} \frac{\Gamma t_m}{1 - e^{-\Gamma t_m}} \left[e^{i\chi t_m/2} \text{sinc}(\chi t_m/2) * \frac{1}{(i\chi - \Gamma)} \right] (\chi)$. For the experimentally relevant limit of a small transmon decay rate, i.e., $\Gamma \ll t_m^{-1}, \chi$, we obtain the approximation $C^{(1)} \approx e^{i(\chi t_m/2 + \theta_0 + \tilde{\theta})} \text{sinc}(\chi t_m/2)$, corresponding to equation (2) in the main text. The optimal feedback phase is therefore $\tilde{\theta}_{\text{opt}} = -\frac{\chi t_m}{2} \bmod \pi - \theta_0$. In this limit, excitations without subsequent spontaneous decay (i.e., event 1) are the dominant contributor to dephasing, yielding a cavity dephasing rate

$$\Gamma_{\phi,\text{fb}}^c \approx \Gamma_{\phi,1}^c \approx \Gamma_{\uparrow} (1 - |\text{sinc}(\chi t_m/2)|). \quad (8)$$

This expression is used in equation (3) of the main text. Had we not applied any phase correction, i.e., $\tilde{\theta} = 0$, we would obtain instead $\Gamma_{\phi,\text{fb}}^c \approx \Gamma_{\uparrow} (1 - \text{sinc}(\chi t_m))$, where we neglected the offset phase. For frequent measurements $\chi t_m \ll 1$, the phase correction therefore results in a fourfold reduction in decoherence.

- In the third and final event, an excitation occurs, but it decays before the transmon is measured. This happens with a probability $p_2 = 1 - p_0 - p_1 = \Gamma_{\uparrow} t_m \left(1 - \frac{1 - e^{-\Gamma t_m}}{\Gamma t_m} \right)$. The corresponding probability distribution $f_{T_1}^{(2)}(\tau_1)$ is obtained by summing over probabilities of events in which the excitation occurred at a time $s = [0, t_m - \tau_1]$ and lasted for a duration τ_1 :

$$f_{T_1}^{(2)}(\tau_1) = \frac{1}{p_2} \int_{s=0}^{t_m - \tau_1} \Gamma_{\uparrow} e^{-\Gamma \tau_1} \Gamma ds = \frac{1}{p_2} \Gamma_{\uparrow} \Gamma (t_m - \tau_1) e^{-\Gamma \tau_1}.$$

The resulting coherence is

$$C^{(2)} = \frac{\Gamma_{\uparrow} \Gamma}{p_2} \frac{[e^{(i\chi - \Gamma)t_m} - 1 - (i\chi - \Gamma)t_m]}{(i\chi - \Gamma)^2}. \quad (9)$$

No feedback is applied for this event, as the transmon decays before the excitation can be observed. In the limit of

infrequent measurements $t_m^{-1} \ll \Gamma, \chi$, this event dominates the dephasing rate, and we retrieve the no-feedback coherence of equation (1) in the main text:

$$\Gamma_{\phi, \text{fb}}^c \approx \Gamma_{\phi, 2}^c \approx \Gamma_{\uparrow} \frac{\chi^2}{\chi^2 + \Gamma^2}. \quad (10)$$

B. Performance of the feedback protocol

In Fig. 5, we show the predicted dephasing time $T_{\phi, \text{fb}}^c = 1/\Gamma_{\phi, \text{fb}}^c$ as a function of χ and t_m , comparing the performance of the optimal phase feedback to that without phase feedback. With the parameters of our experimental system, we obtain dephasing times of 122 ms and 35 ms with and without phase feedback, respectively. The dephasing time in both cases is mostly limited by events of type (1), which account for 96% of all excitation events. Postselecting on zero detections, i.e., considering only events of type (2), the dephasing time increases to 1.7 s. In practice, the measured postselected dephasing time is lower due to readout-induced shot noise dephasing. It is also apparent that a modest increase in the measurement rate can yield dephasing times close to a second without compromising on the dispersive interaction strength.

IV. MEASUREMENT ERRORS

In this section, we modify the expressions derived above to account for non-ideal measurements. The first non-ideality we include is measurement-induced dephasing due to photon shot noise in the readout resonator. In essence, the non-zero cross-Kerr interaction between the readout resonator and the cavity $\chi_{\text{cr}}/2\pi = 552 \pm 18$ Hz causes the readout pulse to weakly measure the cavity state. The cavity decoherence due to a single measurement is extracted from the residual dephasing after postselecting on no excitations (see Fig. 3e in the main text), yielding $1 - C_{\text{RO}} = \frac{2.6 \mu\text{s}}{182 \text{ms}} = 1.4 \times 10^{-5}$. The phenomenological parameter C_{RO} depends on the photon population of the readout resonator during the measurement, as well as the measurement duration. This source of decoherence can be further mitigated by improving the efficiency of the measurement chain.

The second non-ideality we consider is imperfect readout fidelity. We distinguish two main types of readout errors: a false negative (positive) event occurs when a transmon in the excited (ground) state is incorrectly identified as being in the ground (excited) state. This effect is due to the finite overlap between the measurement outcome distributions of the ground and excited states. The probabilities of these events are denoted by $p_{g|e} = 1 - p_{e|e}$ and $p_{e|g} = 1 - p_{g|g}$, respectively. False positives and negatives can be adjusted through a trade-off by modifying the decision boundary for determining the measurement outcomes $|g\rangle$ and $|e\rangle$. Since false positives are more detrimental, we set $p_{e|g} = 2.16 \times 10^{-4}$ and $p_{g|e} = 1.4 \times 10^{-2}$. In the case of incorrect identification, the phase feedback and reset pulse are applied when they shouldn't, and vice versa. As a result, the transmon will spend the subsequent interval t_m in the excited state, assuming no further errors occur. Measurement errors, therefore, lead to unwanted phase accumulations in the subsequent interval, which we consider when deriving the coherence. While the effect of measurement errors on the subsequent interval violates the independence assumption used to derive the cavity dephasing rate, the error introduced by this assumption is only a small second-order effect and can be ignored.

Finally, we consider a gap $t_g = 1.24 \mu\text{s}$ between the detection time and the reset pulse (see Fig. 6). This gap encapsulates the

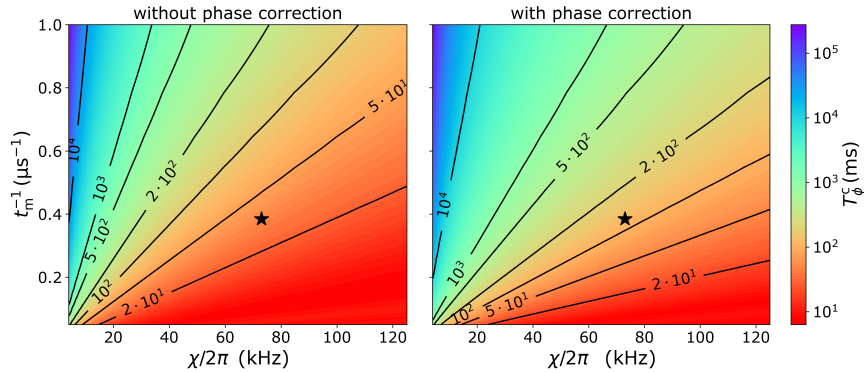


FIG. 5. **Dephasing time with and without phase correction.** Dephasing time versus the dispersive interaction rate χ and the transmon measurement rate t_m^{-1} without (left panel) and with (right panel) cavity phase correction. The star denotes the dephasing time for the parameters from this work, namely $\chi/2\pi = 73$ MHz and $t_m^{-1} = (2.6 \text{ms})^{-1}$.

combined effects of the finite readout duration ($t_{\text{RO}} = 1.6 \mu\text{s}$), the feedback latency ($t_l = 372 \text{ ns}$), and the reset pulse duration ($t_p = 128 \text{ ns}$). The gap results in a deterministic cavity phase accumulation if the transmon is excited at the time of the detection. Moreover, the transmon can decay during this gap period, causing the reset pulse to re-excite the transmon.

We now enumerate the possible events using the same numbered notation as in the previous section, with letters added to denote particular measurement outcomes.

0. a) No excitation occurs, and the state is correctly detected as $|g\rangle$. This is the most likely event, with probability $p_{0a} = (1 - \Gamma_{\uparrow} t_m) p_{g|g}$. The coherence is affected due to readout-induced shot noise dephasing, yielding $C^{(0a)} = C_{\text{RO}}$.
- b) No excitation occurs, but the state is incorrectly identified as $|e\rangle$. The associated probability is $p_{0b} = (1 - \Gamma_{\uparrow} t_m) p_{e|g}$. The reset pulse excites the transmon to $|e\rangle$, where it remains for a duration t_m assuming no decay occurs. The subsequent measurement correctly identifies the state as $|e\rangle$ and the transmon is reset to $|g\rangle$. Hence, the feedback phase is applied twice, while the offset phase is applied only once. The coherence is therefore $C^{(0b)} = C_{\text{RO}} e^{i(2\tilde{\theta} + \chi t_m + \theta_0)}$. Such false-positive events result in an effective heating of the transmon at a rate $\frac{p_{e|g}}{t_m}$, acting as an independent cavity dephasing mechanism to thermal excitations. However, since the phase feedback for the dominant event (1a, see below) is approximately $\tilde{\theta} \approx -(\frac{\chi t_m}{2} + \theta_0 + \chi t_g)$, the phase $\chi t_m + \theta_0$ acquired per false positive is partially mitigated by the application of the twofold phase feedback $2\tilde{\theta}$.
1. a) The transmon is excited, and does not decay. The excitation is correctly identified during the measurement, and does not decay during the gap period. The associated probability and coherence are $p_{1a} = p_1 p_{e|e} e^{-\Gamma t_g}$ and $C^{(1a)} = C_{\text{RO}} C^{(1)} e^{i\chi t_g}$, where $p_1, C^{(1)}$ are the probability and coherence derived for this event with ideal measurement in the previous section, and χt_g is the phase acquired during the gap period before the transmon is reset to $|g\rangle$.
- b) The transmon is excited, and does not decay, but the excitation is incorrectly identified as $|g\rangle$ during the measurement. This event occurs with a probability $p_{1b} = p_1 p_{g|e} e^{-\Gamma t_g}$. The phase feedback is applied after the subsequent interval. The coherence is therefore $C^{(1b)} = C_{\text{RO}} C^{(1)} e^{i(\chi(t_m + t_g) + \theta_0)}$.
- c) The transmon is excited, and does not decay. The excitation is correctly identified during the measurement, but it decays during the gap period. On average, the transmon spends another period $t_g/2$ in its excited state, decays, and is then re-excited by the reset pulse. The probability of this event is $p_{1c} = p_1 p_{e|e} (1 - e^{-\Gamma t_g})$. The feedback and offset phases are applied twice and the associated coherence is $C^{(1c)} = C_{\text{RO}} C^{(1)} e^{i(\tilde{\theta} + \chi(t_m + t_g/2) + \theta_0)}$.
2. a) An excitation occurs, but it decays before the transmon is measured and correctly identified as $|g\rangle$. This happens with a probability $p_{2a} = p_2 p_{g|g}$. The corresponding coherence is $C^{(2a)} = C_{\text{RO}} C^{(2)}$.
- b) An excitation occurs, but decays before the transmon is measured. The state is incorrectly identified as $|e\rangle$, resulting in the application of two feedback phases and a single offset phase. The probability is $p_{2b} = p_2 p_{e|g}$ and the coherence is $C^{(2b)} = C_{\text{RO}} C^{(2)} e^{i(2\tilde{\theta} + \chi t_m + \theta_0)}$. The probability of this event is negligible, but we mention it for completeness.

As in the previous section, the total cavity dephasing is given by

$$\Gamma_{\phi, \text{fb}}^c = \frac{1}{t_m} \sum_i p_i \left(1 - |C^{(i)}| \cos(\tilde{\theta}^{(i)}) \right), \quad (11)$$

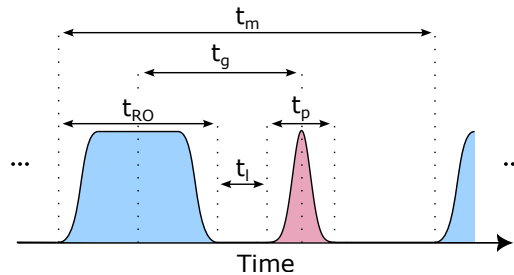


FIG. 6. **Timing diagram of the coherence recovery protocol.** Measurement pulses, shown in blue, have a duration of $t_{\text{RO}} = 1.6 \mu\text{s}$, with transmon state inference occurring on average at the pulse's midpoint. The latency ($t_l = 372 \text{ ns}$) between the end of the measurement pulse and the start of the conditional reset pulse ($t_p = 128 \text{ ns}$) is attributed to processing and signal propagation delays. The gap time, $t_g = \frac{t_{\text{RO}}}{2} + t_l + \frac{t_p}{2}$, marks the duration between the transmon state inference and the midpoint of the reset pulse. The time between measurements $t_m \geq t_{\text{RO}} + t_l + t_p$, is independently set for each experiment.

where $\bar{\theta}^{(i)} = \arg(C^{(i)})$. The optimal feedback phase now has to strike a balance between the various events described above. Writing $\bar{\theta}^{(i)} = \bar{\theta}_0^{(i)} + \alpha_i \tilde{\theta}$, with $\bar{\theta}_0^{(i)}$ the zero-feedback coherence phase of the i^{th} event and α_i the prefactor of the feedback phase for that event as derived above, we can find the optimal angle by solving for $\partial_{\tilde{\theta}} \Gamma_{\phi, \text{fb}}^c = 0$. This procedure yields

$$\tilde{\theta}_{\text{opt}} = - \frac{\sum_i p_i |C^{(i)}| \alpha_i \bar{\theta}_0^{(i)}}{\sum_i p_i |C^{(i)}| \alpha_i^2}, \quad (12)$$

where we used the approximation $\sin(\bar{\theta}^{(i)}) \sim \bar{\theta}^{(i)}$, which is valid for short readout intervals. In Fig. 7, we show the contribution of each dephasing mechanism when using the optimal phase feedback.

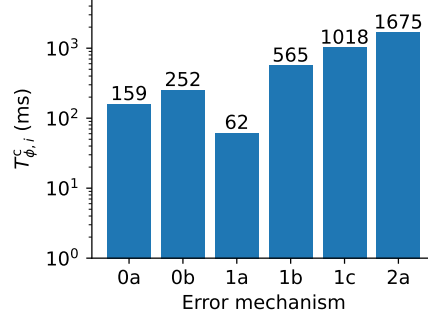


FIG. 7. **Cavity dephasing error budget.** The lifetime of each mechanism $T_{\phi,i}^c = 1/\Gamma_{\phi,i}^c$ is shown according to the listing in section D. We use the experimental parameters outlined in Table 1, and the optimal phase calculated from equation (12). The total lifetime is $T_{\phi}^c = 1/\sum \Gamma_{\phi,i}^c = 33.5$ ms.

V. UNCERTAINTY IN DECAY TIME

In Fig. 2 of the main text, we explored the decoherence due to a single excitation after initializing the transmon in $|g\rangle$. In this section, we explore the opposite scenario: we prepare the transmon in $|e\rangle$ and postselect on observing $|g\rangle$, leaving only those experimental runs in which a relaxation event occurred (see Fig. 8a). Fig. 8b shows the resulting cavity coherence as a function of t_m . Since the decay rate is much higher than the excitation rate, this experiment has a much better signal-to-noise ratio than its counterpart in Fig. 2b of the main text.

The probability density for the excitation duration in this scenario is given by

$$f_T(\tau) = \frac{\Gamma e^{-\Gamma\tau}}{1 - e^{-\Gamma t_m}},$$

and the corresponding cavity coherence is

$$C_1 = \int_{\tau=0}^{t_m} e^{i\chi\tau} f_T(\tau) d\tau = \frac{\Gamma}{1 - e^{-\Gamma t_m}} \frac{e^{(i\chi - \Gamma)t_m} - 1}{i\chi - \Gamma}. \quad (13)$$

This coherence is in excellent agreement with the data in Fig. 8b.

VI. HIDDEN MARKOV MODEL

The repeated transmon measurements can potentially modify the system parameters. To characterize the system during the measurement protocol, we use a hidden Markov model (HMM), enabling us to infer the transmon transition probabilities as well as the measurement errors. In the following sections, we introduce the HMM, establish inference functions to estimate the transmon state, and demonstrate the parameter estimation procedure, as well as the reconstruction of the transmon states from the measurement outcomes.

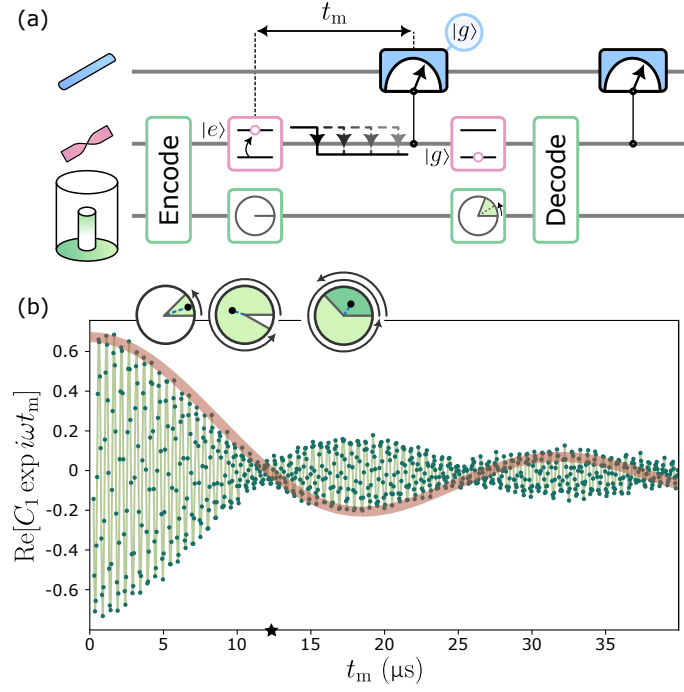


FIG. 8. **Cavity's coherence with induced ancilla error.** **a**, Circuit for observing cavity decoherence from a single transmon relaxation event. The transmon is initialized in its excited state, and the cavity is encoded in a superposition state $\frac{1}{\sqrt{2}}(|0\rangle + |1\rangle)$. After a time t_m , we measure the transmon and decode the cavity state postselecting on the observation of the transmon in its ground state. **b**, Real part of the coherence of the cavity state as a function of the measurement time t_m (green markers). For clarity, we used a frame in which the cavity rotates at a frequency $\omega = 1.950 \pm 0.95$ MHz. The brown curve shows the real part of the coherence in a non-rotating frame derived in equation (13). The measurement interval corresponding to $t_m = 2\pi/\chi$ is indicated by a black star. The insets illustrate the equatorial plane of the cavity qubit's Bloch sphere with the phase distribution in green and the coherence indicated by a black dot. We use the experimental parameters from Fig. 2 in the main text and normalize the coherence to take into account the loss in contrast.

A. Statistical model - free evolution

We aim to construct a model that accurately captures the time-dependent state evolution of a two-level transmon. Considering the memoryless nature of transmon evolution, a Markov model is a straightforward choice, as it assumes the future state depends only on the current state, not on the sequence of events that preceded it. This model can then be used to infer the system parameters based on the transmon evolution observed at discrete time steps. However, our observations are generated from an imperfect measurement device with a non-zero probability of false positives and false negatives. For this reason, we use a Hidden Markov Model (HMM), where the transmon state at each time step is represented by a hidden variable x we don't have direct access to. The HMM is defined by three parameters:

1. Transition matrix: determines the likelihood of the hidden state at the n^{th} time step, based on the hidden state's probability at the previous time step:

$$T_{ij} \equiv p(x_n = j | x_{n-1} = i).$$

We express the transition matrix using the probabilities for excitation $p_{\uparrow} = \Gamma_{\uparrow} t_m$ and relaxation $p_{\downarrow} = 1 - e^{-\Gamma_{\downarrow} t_m}$:

$$T = \begin{pmatrix} 1 - p_{\uparrow} & p_{\uparrow} \\ p_{\downarrow} & 1 - p_{\downarrow} \end{pmatrix}$$

We denote the hidden state at time i as x_i , and the collection of states between times i and j as $x_{i:j}$.

2. Emission matrix: we denote the observation at time i as o_i , and the collection of observations between times i and j as $o_{i:j}$.

We use an indicator column vector to describe the observations:

$$\gamma(o_i) = \begin{cases} (1, 0)^T & \text{if } o_i = 0 \\ (0, 1)^T & \text{if } o_i = 1. \end{cases}$$

To describe the imperfect measurement, we define an emission matrix

$$M = \begin{pmatrix} 1 - p_{e|g} & p_{e|g} \\ p_{g|e} & 1 - p_{g|e} \end{pmatrix},$$

where $p_{e|g}$ and $p_{g|e}$ are the probabilities for false-positive and false-negative observations. We can express the probability of obtaining the outcome o_n :

$$p(o_n | x_n = j) = \sum_k M_{jk} \cdot \gamma(o_n)_k.$$

3. Initial vector: this vector, denoted by π , describes the probability of the hidden state at the onset of the evolution.

B. Inference - likelihood and smoothed values

Next, we derive a statistical inference model to estimate the HMM parameters. Specifically, we aim to reconstruct the matrices T, M by finding the set of parameters $\lambda = \{p_{e|g}, p_{g|e}, \Gamma_{\uparrow}, \Gamma\}$ that best explain the observed data. Formally, we want to maximize the posterior distribution. The optimal estimate $\bar{\lambda}$ satisfies

$$\bar{\lambda} = \arg \max_{\lambda} [p(\lambda | o_{1:N})] = \arg \max_{\lambda} [\mathcal{L}_{\lambda}(o_{1:N}) \cdot p(\lambda)] \approx \arg \max_{\lambda} [\mathcal{L}_{\lambda}(o_{1:N})],$$

where the likelihood \mathcal{L}_{λ} that λ matches the observations $(o_{1:N})$ and N is the final time step. We can derive the likelihood by establishing a recursive relation by either going forward (from start to end) or backward (from end to start):

1. forward -

$$\mathcal{L}_{\lambda}(o_{1:N}) \equiv p(o_{1:N} | \lambda) = \sum_{x_N} p(o_{1:N}, x_N | \lambda) \equiv \sum_i f_i(N),$$

where the forward vector $f_i(k)$ is the joint probability of the hidden state at time k being i and the observations up to time k . We can now expand the forward vector recursively using the emission and transition matrices:

$$f_i(k) = \sum_{l,j} \gamma(o_k)_l \cdot M_{il} \cdot T_{ji} \cdot f_j(k-1),$$

where the initial condition is $f_i(0) = \pi_i$. Next, we introduce a forward vector that is normalized at each time step, denoted by $\hat{f}_i(k) \equiv \frac{f_i(k)}{f_0(k) + f_1(k)}$. We can express the normalized forward vector recursively:

$$\hat{f}_i(k) = c_k^{-1} \sum_{l,j} \gamma(o_k)_l \cdot M_{il} \cdot T_{ji} \cdot \hat{f}_j(k-1) = \frac{f_i(k)}{\prod_{s=1}^k c_s},$$

where c_k is a normalization scalar derived from the recursive relation:

$$c_k = \sum_i \sum_{l,j} \gamma(o_k)_l \cdot M_{il} \cdot T_{ji} \cdot \hat{f}_j(k-1).$$

2. backward -

$$\mathcal{L}_{\lambda}(o_{1:N}) \equiv p(o_{1:N} | \lambda) = \sum_i p(o_{1:N} | x_0 = i, \lambda) \cdot p(x_0 = i | \lambda) \equiv \sum_i b_i(0) \cdot \pi_i,$$

where the backward vector $b_i(k)$ is the probability vector of the observations from time $k+1$ until the final time step,

given that the hidden state at time k is equal to i :

$$b_i(k) = p(o_{k+1:N} | x_k = i, \lambda) = \sum_{j,l} \gamma(o_{k+1})_l \cdot M_{jl} \cdot T_{ij} \cdot b_j(k+1),$$

where the boundary condition is $b_i(N) = (1, 1)$. Similarly to the forward vector, we can normalize the backward vector at each time step, denoting the normalization coefficient as c_{k+1} . We then obtain for each time step k :

$$\hat{b}_i(k) = c_{k+1}^{-1} \sum_{j,l} \gamma(o_{k+1})_l \cdot M_{jl} \cdot T_{ij} \cdot \hat{b}_j(k+1) = \frac{b_i(k)}{\prod_{s=k+1}^N c_s}.$$

Finally, we can combine both forward and backward vectors to compute a ‘‘smoothed value’’ for the hidden variable at time step k . Formally, we denote $\omega_i(k)$ as the probability for $x_k = i$ given all available observations:

$$\omega_i(k) = p(x_k = i | o_{1:N}, \pi) = \frac{p(x_k = i, o_{1:N} | \pi)}{p(o_{1:N} | \pi)} = \frac{b_i(k) \cdot f_i(k)}{\sum_i b_i(k) \cdot f_i(k)} = \hat{b}_i(k) \cdot \hat{f}_i(k).$$

Using the smoothed values we can estimate the most probable hidden states of the transmon given a set of system parameters and observations. Conversely, the smoothed values can be used to estimate the system parameters using an optimization algorithm. In essence, such an algorithm estimates the hidden state given a set of observations, updates the system parameters accordingly, and repeats this process.

C. Parameter estimation and reconstruction

We choose the Baum-Welch algorithm for finding the parameters that best explain the observations. The Baum-Welch algorithm is an expectation-maximization algorithm suitable for HMM that uses both forward and backward vectors. The parameter estimation process starts by recording the trajectory of the transmon using repeated measurements. We then feed the optimizer the observed data, obtaining the most likely model parameters $\{p_{e|g}, p_{g|e}, \Gamma_{\uparrow}, \Gamma\}$. We show an example of this process in Fig. 9, where we use simulated data. Using the estimated parameters, we can next compute the smoothed values, yielding the most likely trajectory of the transmon state.

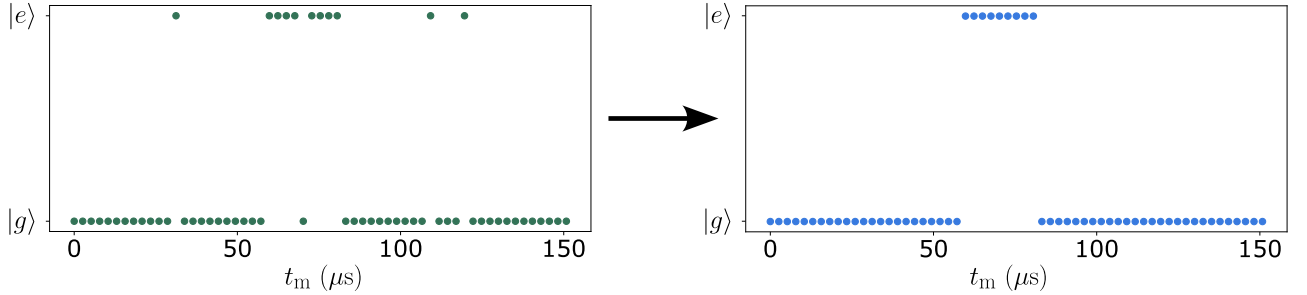


FIG. 9. **Markov estimation and reconstruction procedure.** The left panel shows a simulated set of observations. The right panel demonstrates the reconstructed state after estimating the parameters from the observations. In particular, the reconstruction successfully identifies three false positive events, a single transmon excitation, and a single false negative event. The time between measurements is $t_m = 2.6 \mu\text{s}$. The parameters estimated from the simulated observations are: $p_{e|g} = 6\%$, $p_{g|e} = 14\%$, $\Gamma = 56 \text{ kHz}$, and $\Gamma_{\uparrow} = 10 \text{ kHz}$.

We use the parameter extraction procedure for various applications. For example, we extract the excitation rate induced by the incoherent transmon drive (see Fig. 4b in the main text). In addition, we can incorporate the state reconstruction process as part of the coherence recovery protocol. That is, instead of conditioning the transmon reset and phase correction at each time step on the current observation, we can use all previous measurements to decide on the best course of action. This method offers several advantages. We can aggregate several observations to acquire a higher degree of confidence before applying a reset pulse. Moreover, we can identify false positives and false negatives in retrospect, and apply phase corrections to compensate for these events.

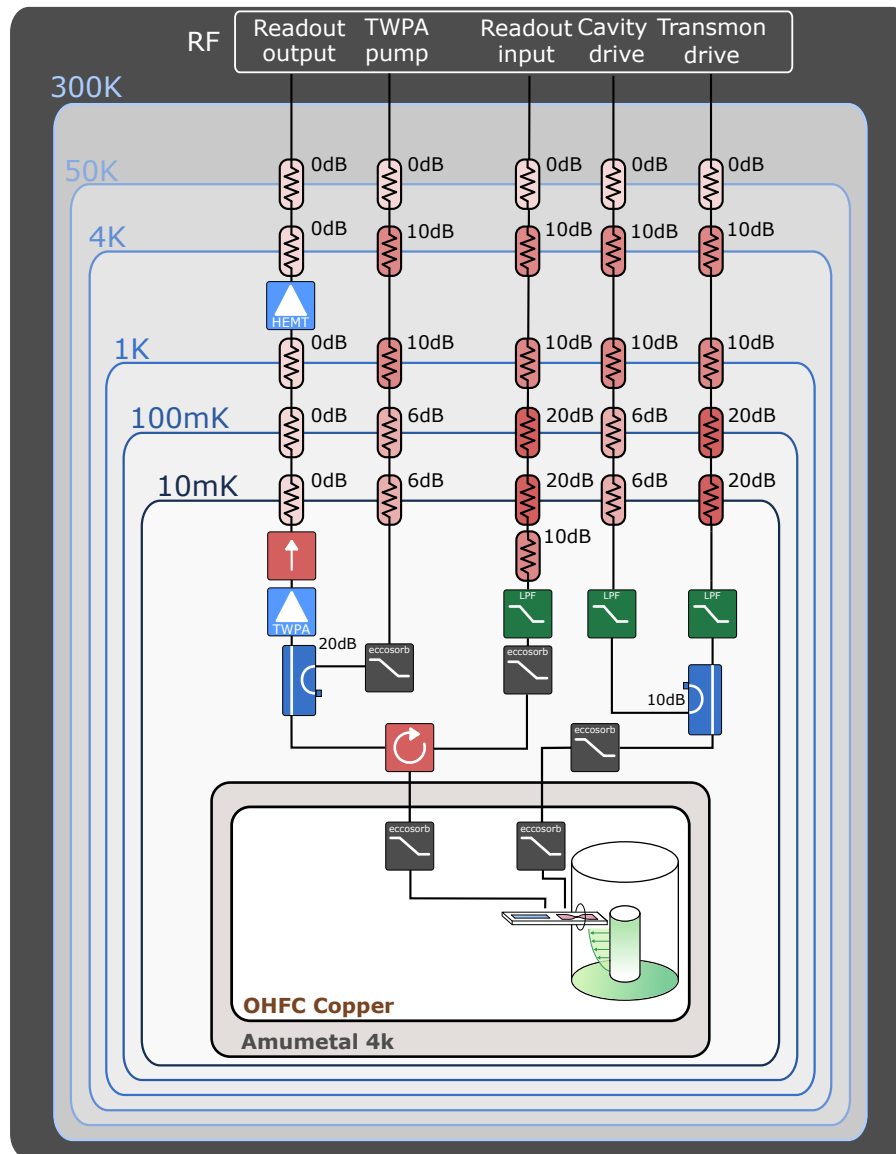


FIG. 10. **Wiring diagram of the cryogenic microwave setup.** The experimental device is placed inside OFHC and A4K shields. The control signals are generated using Quantum Machines' OPX+ system and upconverted using IQ mixers. The signals are passed through a series of attenuators, low pass filters (LPF), and Eccosorb infrared filters. The output signal is amplified by a traveling wave parametric amplifier (TWPA) from Silent Waves before passing through a double-junction isolator, enabling high-fidelity single-shot measurements.